2015

Tomographic imaging of nonsymmetric multicomponent tailored supersonic flows from structured gas nozzles

Grigory V. Golovin
University of Nebraska-Lincoln, ggolovin2@unl.edu

Sudeep Banerjee
University of Nebraska-Lincoln, sbanejee2@unl.edu

J Zhang
University of Nebraska-Lincoln

Shouyuan Chen
University of Nebraska-Lincoln, schen6@unl.edu

Cheng Liu
University of Nebraska-Lincoln, cliu8@unl.edu

See next page for additional authors

applied optics

Tomographic imaging of nonsymmetric multicomponent tailored supersonic flows from structured gas nozzles

G. Golovin, S. Banerjee, J. Zhang, S. Chen, C. Liu, B. Zhao, J. Mills, K. Brown, C. Petersen, and D. Umstadter*

Department of Physics and Astronomy, University of Nebraska, Lincoln, Nebraska 68588, USA
**Corresponding author: donald.umstadter@unl.edu*

Received 8 October 2014; revised 13 March 2015; accepted 13 March 2015; posted 13 March 2015 (Doc. ID 224435); published 10 April 2015

We report experimental results on the production and characterization of asymmetric and composite supersonic gas flows, created by merging independently controllable flows from multiple nozzles. We demonstrate that the spatial profiles are adjustable over a large range of parameters, including gas density, density gradient, and atomic composition. The profiles were precisely characterized using three-dimensional tomography. The creation and measurement of complex gas flows is relevant to numerous applications, ranging from laser-produced plasmas to rocket thrusters.

OCIS codes: (120.3180) Interferometry; (110.6955) Tomographic imaging; (280.5395) Plasma diagnostics.

http://dx.doi.org/10.1364/AO.54.003491

1. INTRODUCTION

Gas jets are widely used in many areas of modern science and industry, ranging from aircraft propulsion systems [1] to microjet arrays [2], and span a range of sizes. They are employed in conventional radio-frequency accelerators for nuclear spectroscopy measurements, in pulsed x-ray machines to create hot plasma pinch, and in the investigation of inertial confinement fusion [3]. There has been extensive use of gas jets in studies of laser–plasma interactions, such as generation of high harmonics [4], THz [5], extreme ultraviolet radiation [6], x-rays [7], and ion beams [8]. Underdense plasma targets based on gas jets have been used for laser pulse compression [9], laser frequency upshift [10], and smoothing of the laser beam intensity fluctuation [11]. The rapidly expanding field of laser wakefield acceleration relies on the use of supersonic gas jets in order to drive wakes and produce energetic electron beams using high-intensity laser pulses [12,13]. There is now an increasing trend to replace the standard Laval nozzle with complex jets to precisely tailor the density profile so that the process of electron injection can be localized, leading to better control of electron acceleration [14,15]. Gas jets are also used in laser-driven high-energy x-ray sources based on inverse Compton scattering [16–19].

For the purpose of designing targets for experiments, as well as engineering gas flows for applications, precise measurement of the absolute density and density profile is a critical requirement. The techniques of interferometry, Schlieren imaging, and shadowgraphy provide the integrated (along the propagation axis) refractive index, and its first and second derivatives [20], respectively. In the case of a cylindrically symmetric jet, integrated information along one axis is sufficient to reconstruct the 3D density profile using inversion techniques such as the Abel transform [21–26]. However, when flows are not cylindrically symmetric, reconstruction of the gas flow pattern requires the use of more complex tomographic methods. In general, multiple measurements of the flow along different axes are combined, and the 3D density map is extracted using mathematical procedures such as filtered backprojection [27] or algebraic reconstruction techniques (ART) [28]. Often, some modifications of general ART are used, such as averaging ART (AVART) [29] or simultaneous iterative reconstruction technique (SIRT) [30,31]. Tomographic measurements are also needed for superposed or colliding flows, or when the initially symmetric gas flow is perturbed by inserting wires [32] or other obstacles [33], or by machining with a high-intensity laser pulse [34,35]. Such perturbed and tailored density profiles are currently of great interest. For instance, they have been shown to allow controlled electron injection in laser-produced plasma wakes [36–40] and have led to significant recent advances in this important emerging area.

In this paper, we perform tomographic measurements and use SIRT to reconstruct the 3D density map of an asymmetric gas target in a vacuum. The target was created by two expanding jets, which merged into a composite flow above the nozzle orifice. We studied the interaction of the gas flows and

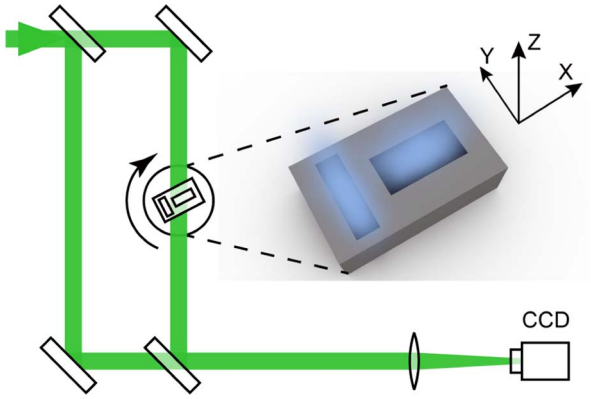

Fig. 1. Experimental setup. Double-nozzle target is installed on a rotation stage in one arm of a Mach–Zehnder interferometer. First and second Laval nozzles of the gas target have 2 mm × 0.5 mm and 1 mm × 2 mm rectangular openings, respectively.

investigated the degree of control that is possible for the gas profile in the region where the flows overlap. These tailored gas density profiles permit independent control over density-dependent processes, such as electron injection and acceleration in laser-wakefield electron accelerators [17,41]. More generally, this technique is applicable whenever precise characterization of complex 3D flows is required.

2. EXPERIMENTAL SETUP AND METHODS

In order to perform tomographic measurements of the gas profile from the jet, we implemented a Mach–Zehnder interferometer, as shown in Fig. 1. The illumination source was 532 nm light from a frequency-doubled Nd:YAG laser (SAGA PRO 230/10 SHG, 5.2 ns pulse duration, 10 Hz repetition rate). Two slit nozzles (also referred to as a double-jet) with 0.5 mm × 2 mm and 2 mm × 1 mm openings and separated by a 0.5 mm gap, formed the gas target. The double-jet was placed in one arm of the interferometer. The entire assembly is housed in a vacuum chamber at a base pressure of 50 mTorr. The gas jet density is proportional to the phase shift introduced in the fringe pattern produced by the interference of the two beams and is recorded using a 12-bit CCD camera. The double-jet was mounted on a rotation stage and interferograms were recorded for two angles between the gas target and the laser beam (0° and 90°). In the subsequent section, we will demonstrate that the use of two angles is sufficient to reconstruct the profile for this particular jet on account of the axis of symmetry associated with it. Pure nitrogen is used for these measurements because it has a large refractive index, and, as a result, a significant phase shift is produced.

We extracted the phase shift from the interferograms in four steps. Figure 2(a) gives an example of a raw interferogram. First, we transformed it to the frequency domain by means of a 2D Fourier transform [the result is shown in Fig. 2(b)]. We then applied a spatial filter, which limited the 2D spectrum to a rectangular box [shown as the white rectangular overlay in Fig. 2(b)]. The size of the rectangular filter determines the resolution of the measurement. A larger box leads to finer resolution, but limiting the size of this region permits mitigation of distortions in the original interferogram caused by imperfections in the beam. Next, we performed an inverse Fourier transform to the filtered 2D spectrum, which resulted in a phase shift with discontinuities [Fig. 2(c)]. Finally, we applied a 1D unwrapping algorithm (to each column of the phase shift) to obtain a continuous phase-shift map [Fig. 2(d)]. We also compared the results obtained using our unwrapping algorithm with the 2D Goldstein unwrapping [42] and found that both algorithms gave the same results, proving that our reconstruction is robust.

The phase shift φ of a laser pulse with wavelength λ, as it propagates through a medium with a spatially dependent refractive index $n(x)$, is given by

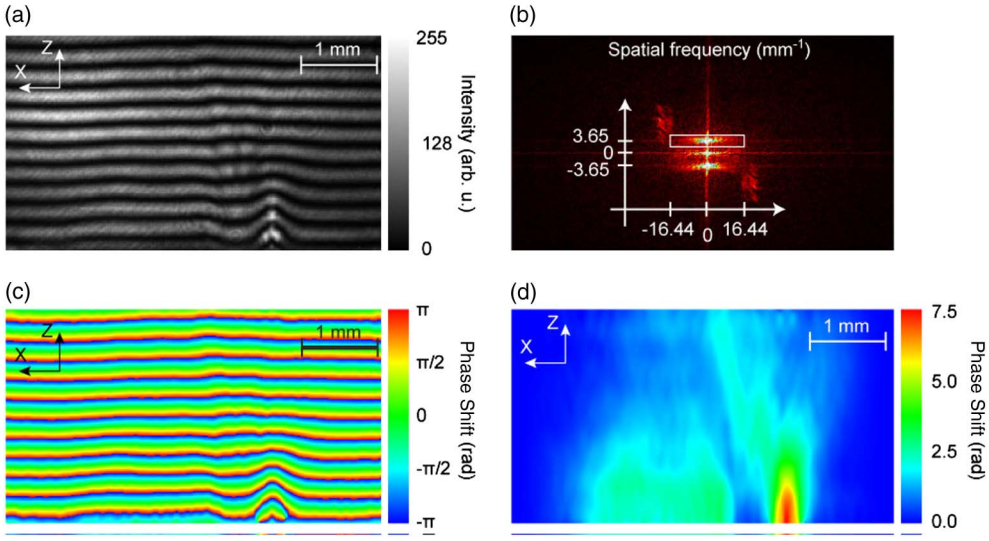

Fig. 2. Interferometry algorithm. (a) Raw interferogram. (b) 2D Fourier spectrum of the raw interferogram (white box shows applied spatial filter). (c) Phase shift with discontinuities. (d) Continuous phase shift. Double jet operated at 150 and 300 PSI backing pressures for the first and second jets, respectively.

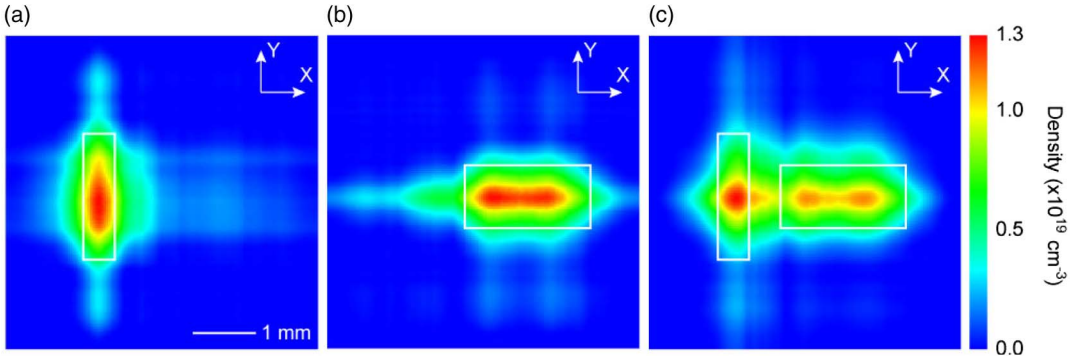

Fig. 3. 2D density maps of the double-jet at 1 mm height above the nozzles orifices, reconstructed with tomography. First and second jets operated at 150 and 300 PSI backing pressures, respectively. (a) First jet only. (b) Second jet only. (c) Both jets. White boxes show nozzle openings.

$$\varphi = \frac{2\pi}{\lambda}\int_0^L [n(x) - 1]\mathrm{d}x,$$

where the integration is performed along the axis of propagation with length L. It is clear from the above that the use of doubled light from the laser improves sensitivity by a factor of two compared to the fundamental wavelength at 1064 nm.

The 2D density maps were reconstructed from the phase shift maps using SIRT algorithm. This was done at different heights from the nozzle opening. By combining these 2D maps for different heights, the full 3D density profile was obtained. The algorithm worked in the following way. The phase-shift ray sum (a phase shift, accumulated by light as it propagates along the ray path) can be expressed as

$$\varphi_{nm} = \sum_{ij}\left[\frac{2\pi}{\lambda}(n_{ij} - n_0)\right] w_{ijnm} = \sum_{ij} f_{ij} w_{ijnm},$$

where the n index specifies angle (thus, for two interferograms made from two different angles, $n = 1, 2$), m index specifies a ray sum within this set (thus, if the interferograms were made with 100 pixels resolution, $m = 1\ldots100$), i and j indexes represent the 2D spatial grid, f_{ij} is the perturbation function, and w_{ijnm} is the area of the (i, j) spatial cell, covered by (n, m) ray. The goal of the algorithm was to find the perturbation function f_{ij}, which would result in the measured ray sums. The algorithm started from an "initial guess" (simply $f_{ij} = 0$) and iterated according to the following strategy:

$$f_{ij}^{(q+1)} = f_{ij}^{(q)} + \alpha\left[\sum_{nm}\left(w_{ijmn} \times \frac{\varphi_{mn} - \sum_{ij} w_{ijmn} f_{ij}^{(q)}}{\sum_{ij} w_{ijmn}}\right)\right] \times \left(\sum_{nm} w_{ijmn}\right)^{-1},$$

where q stands for the iteration number and α is an aggressiveness factor (the algorithm is stable for $0 < \alpha \le 2$). The iteration process continued until the difference between measured ray sums and simulated ones $\varphi_{nm} - \sum_{ij} w_{ijnm} f_{ij}^{(q)}$ was determined to be small enough (less than 1% of the maximum phase shift). To mitigate well-known salt-and-pepper noise, we applied spatial filtering to the intermediate results. Usually, the algorithm made 50–100 iterations to reach the desired accuracy level. After the spatially dependent index n_{ij} of refraction was obtained, we calculated local density using

$$d_{ij} = \frac{2}{3}\left(\frac{n_{ij} - 1}{A}\right),$$

where A is molar refractivity of the gas [43].

3. RESULTS AND DISCUSSION

Tomographic measurements were then performed for the structured jet composed of two slit nozzles (with 0.5 mm × 2 mm and 2 mm × 1 mm openings), separated by 0.5 mm. The gas profile for this target was composed of the overlapped flows from both nozzles. To determine how the flows interact, we measured the gas profiles from each nozzle separately and then compared the result with the combined profile. The 2D density maps for these three cases (first nozzle only, second nozzle only, and both nozzles) are shown in Fig. 3; corresponding density profiles (along the X axis) are shown in Fig. 4. By comparing the black solid curve (both nozzles) and the black dashed curve (a sum of density profiles from individual nozzles) in Fig. 4, it is apparent that the superposition principle applies

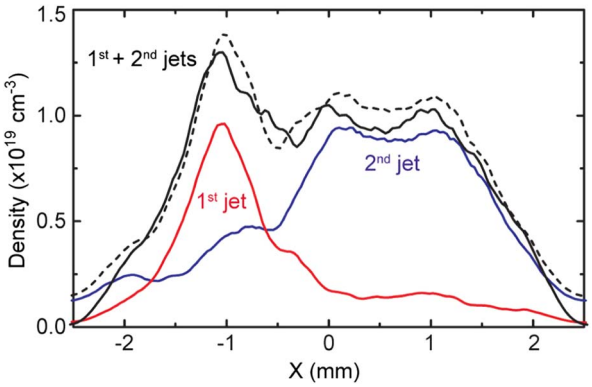

Fig. 4. Longitudinal density profiles of the double-jet at 1 mm height above the nozzles orifices, reconstructed with tomography. First and second jets operated at 150 and 300 PSI backing pressures, respectively. Red curve: first jet only. Blue curve: second jet only. Black solid curve: both jets. Black dashed curve: a sum of first jet only and second jet only density profiles.

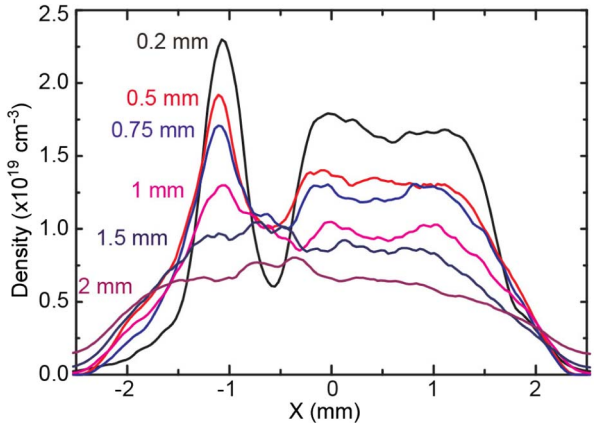

Fig. 5. Longitudinal density profiles of the double jet at different heights above the nozzles orifices, reconstructed with tomography. First and second jets operated at 150 and 300 PSI backing pressures, respectively.

to this case, and the combined density from the two jets is the sum of the individual densities.

The density profiles of the double-nozzle gas target at different heights above the nozzle orifices are shown in Fig. 5. The flows from the two nozzles do not significantly overlap close to the nozzle orifices, as can be seen from the density profile at 0.2 mm height. As the height goes up, the overlap becomes more pronounced, and, at 1.25 mm height and above, there is no clear separation of the flows. This feature of the double-nozzle gas target design is of particular interest for dual-stage laser wakefield acceleration schemes [44]. It provides a simple way to vary the separation of two independently controlled gas flows by appropriate choice of the height at which a laser pulse interacts with the gas target. In addition, it also controls the gradients of the down-ramp and up-ramp between the regions (bigger separation results in sharper ramps), which is also of interest for controlled electron injection on the down-ramp in laser wakefield accelerators [45].

The suitability of the dual-nozzle gas jet design for applications (such as laser wakefield accelerators) depends also on whether it is possible to independently control different stages (flow patterns from each orifice). In order to test the degree of this independence, we scanned the backing pressure of the second nozzle, while holding the backing pressure of the first nozzle constant. As one can see from Figs. 6(a) and 6(b) (corresponding to 0.2 mm height above the nozzle orifices), the density of the plateau region in the second stage changes linearly with the second nozzle backing pressure. At the same

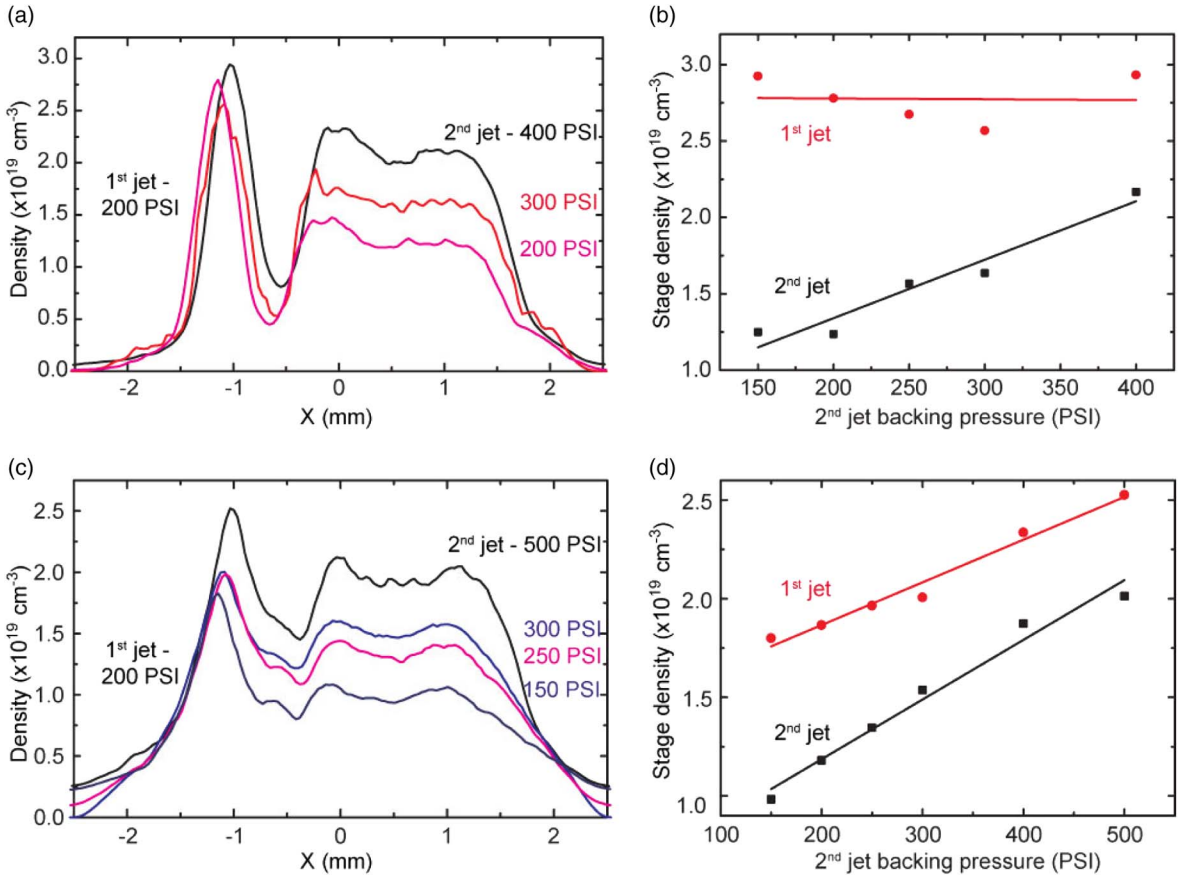

Fig. 6. (a) Longitudinal density profiles of the double jet at 0.2 mm height above the nozzles orifices, reconstructed with tomography. First jet operated at 200 PSI backing pressures. Second jet operated at different backing pressures. (b) Densities of the first stage (from the first nozzle) and the second stage (plateau, the second nozzle) as a function of the second nozzle backing pressure, 0.2 mm height above the nozzle orifices. (c) and (d) are the same but at 0.75 mm height above the nozzle orifices.

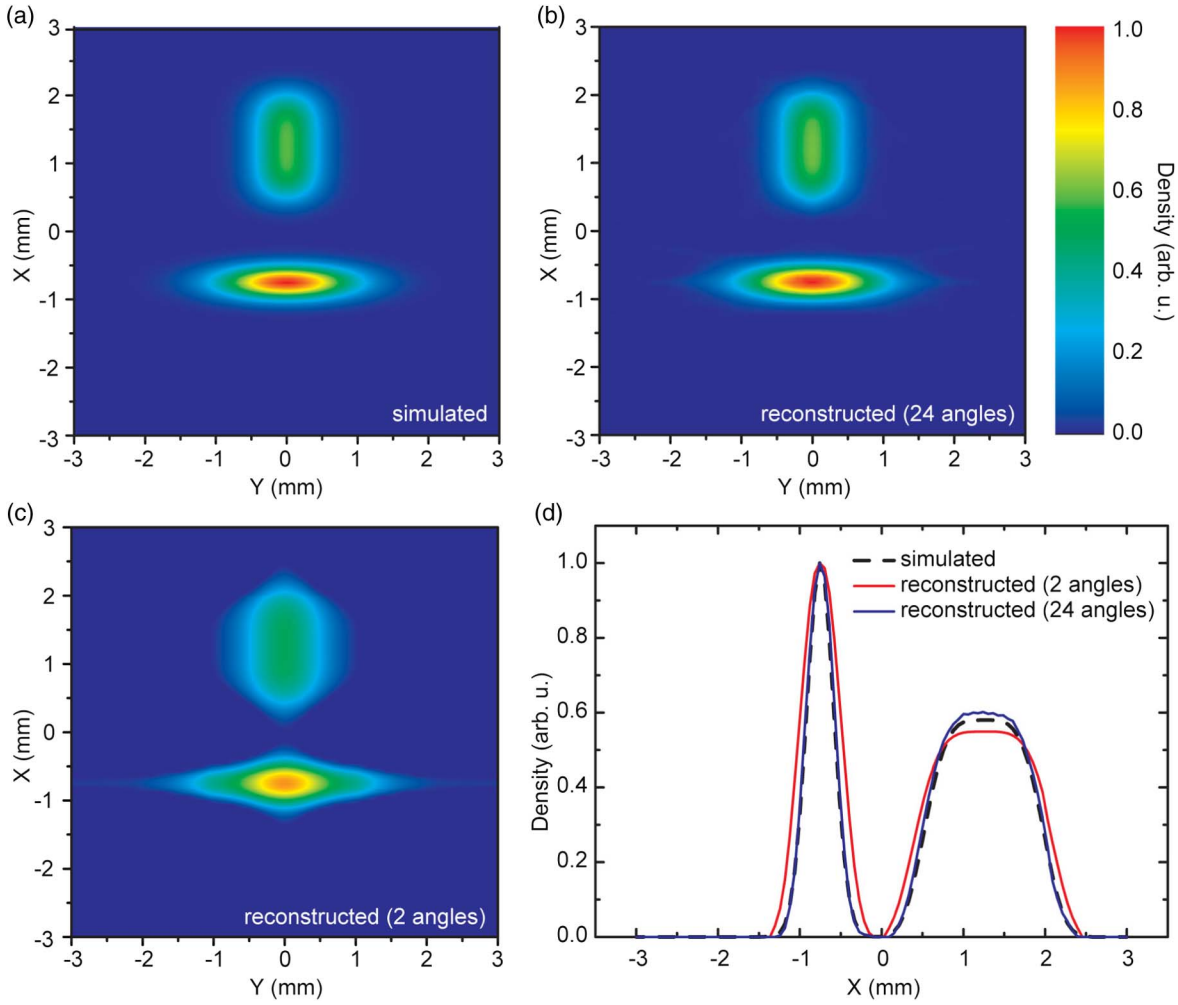

Fig. 7. Tomography reconstruction of a simulated 2D gas density distribution. (a) Simulated distribution. (b) Reconstructed distribution, based on 24 observation angles (0° to 345° with 15° step). (c) Reconstructed distribution, based on two observation angles (0° and 90°). (d) Comparison of simulated and reconstructed longitudinal density profiles (along X direction at $Y = 0$ mm).

time, the density of the first stage also changes, but the change is quite small. Thus, the stages can be controlled independently because the gas flows at this height almost do not overlap (see Fig. 5). Figures 6(c) and 6(d) show the situation when the height is increased to 0.75 mm above the nozzle orifices, which corresponds to significant overlap of the flows. As a result, the densities of both stages change linearly with the second nozzle backing pressure, which means that, in this particular case, the stages cannot be controlled independently.

4. SIMULATIONS

To test the robustness of our results, we simulated the 2D density distribution similar to what is produced by the double-jet [see Fig. 7(a)]. We then simulated phase shift profiles for 24 observation angles (0° to 345° with 15° step) and fed these data to the algorithm. The reconstructed 2D density distribution is shown in Fig. 7(b) and matches perfectly the simulated one, which proves the correctness of the implementation. We then tested the algorithm with not 24, but only two phase-shift profiles (at 0° and 90°). The reconstructed 2D density distribution is shown in Fig. 7(c). It slightly differs from the simulated one, which is not surprising. However, we are mainly interested in longitudinal density profile of the double-jet, since that is the profile a laser pulse "sees" while interacting with the gas target. The comparison of these longitudinal profiles (along X direction at $Y = 0$ mm) is shown in Fig. 7(d). As can be seen, the reconstruction based on only two observation angles is close enough to the simulated density profile. This is due to the axis symmetry of the gas target. This simulation shows the validity of using two orthogonal projections for tomographic reconstruction of the gas profile of the double-jet.

5. CONCLUSIONS

We have presented a detailed study of the gas-flow characteristics from a nonsymmetric, double-nozzle gas target using the tomographic technique. We used interferograms from two perpendicular directions and SIRT algorithm to reconstruct 3D density maps of the target. Our study reveals the characteristics of the flow from such composite targets and its dependence on geometrical parameters. The results of this work can be

used in the design of future laser wakefield accelerators with the goal of producing electron beams with low energy spread and tunable in energy. This can be achieved by localizing the region where electrons are injected and independently controlling the final energy in a flat-top acceleration stage. The general tomography technique can be applied in any area of science or industry where precise 3D measurements of asymmetrical gas jet profiles are required. Future work will extend this technique to the characterization of more complex targets using multiple projections.

Air Force Office of Scientific Research (AFOSR) (FA9550-11-1-0157, high-field laser-electron scattering); National Strategic Research Institute (FA4600-12-D-9000, selective photoactivation analysis); U.S. Department of Energy (DOE) (DE-FG02-05ER15663, ultrafast x-ray science); U.S. Department of Homeland Security (DHS) (HSHQDC-13-C-B0036, low-dose x-ray radiography). This support does not constitute an express or implied endorsement on the part of the government.

We would like to thank Emily Grace and Brock Makovicka for assistance with the experiments and Neelee Glasco for editing the manuscript.

REFERENCES

1. D. Estruch, N. J. Lawson, and K. P. Garry, "Application of optical measurement techniques to supersonic and hypersonic aerospace flows," J. Aerosp. Eng. **22**, 383–395 (2009).
2. S. Y. Yee, R. L. Peterson, L. P. Bernal, and K. Najafi, "High-speed air microjet arrays produced using acoustic streaming for micro propulsion," in *The 17th International Conference on Solid-State Sensors, Actuators and Microsystems (TRANSDUCERS & EUROSENSORS XXVII)* (IEEE, 2013), pp. 1595–1598.
3. J. Denavit and D. W. Phillion, "Laser ionization and heating of gas targets for long-scale-length instability experiments," Phys. Plasmas **1**, 1971–1984 (1994).
4. P. M. Paul, E. S. Toma, P. Breger, G. Mullot, F. Auge, P. Balcou, H. G. Muller, and P. Agostini, "Observation of a train of attosecond pulses from high harmonic generation," Science **292**, 1689–1692 (2001).
5. W. P. Leemans, C. G. R. Geddes, J. Faure, C. Tóth, J. van Tilborg, C. B. Schroeder, E. Esarey, G. Fubiani, D. Auerbach, B. Marcelis, M. A. Carnahan, R. A. Kaindl, J. Byrd, and M. C. Martin, "Observation of terahertz emission from a laser-plasma accelerated electron bunch crossing a plasma-vacuum boundary," Phys. Rev. Lett. **91**, 74802 (2003).
6. T. Sekikawa, A. Kosuge, T. Kanai, and S. Watanabe, "Nonlinear optics in the extreme ultraviolet," Nature **432**, 605–608 (2004).
7. S. Kneip, S. Nagel, C. Bellei, N. Bourgeois, A. Dangor, A. Gopal, R. Heathcote, S. Mangles, J. Marquès, A. Maksimchuk, P. Nilson, K. Phuoc, S. Reed, M. Tzoufras, F. Tsung, L. Willingale, W. Mori, A. Rousse, K. Krushelnick, and Z. Najmudin, "Observation of synchrotron radiation from electrons accelerated in a petawatt-laser-generated plasma cavity," Phys. Rev. Lett. **100**, 105006 (2008).
8. L. Willingale, S. P. D. Mangles, P. M. Nilson, R. J. Clarke, A. E. Dangor, M. C. Kaluza, S. Karsch, K. L. Lancaster, W. B. Mori, Z. Najmudin, J. Schreiber, A. G. R. Thomas, M. S. Wei, and K. Krushelnick, "Collimated multi-MeV ion beams from high-intensity laser interactions with underdense plasma," Phys. Rev. Lett. **96**, 245002 (2006).
9. J. Faure, Y. Glinec, J. Santos, F. Ewald, J.-P. Rousseau, S. Kiselev, A. Pukhov, T. Hosokai, and V. Malka, "Observation of laser-pulse shortening in nonlinear plasma waves," Phys. Rev. Lett. **95**, 1–4 (2005).
10. M. Kando, Y. Fukuda, A. S. Pirozhkov, J. Ma, I. Daito, L.-M. Chen, T. Z. Esirkepov, K. Ogura, T. Homma, Y. Hayashi, H. Kotaki, A. Sagisaka, M. Mori, J. K. Koga, H. Daido, S. V. Bulanov, T. Kimura, Y. Kato, and T. Tajima, "Demonstration of laser-frequency upshift by electron-density modulations in a plasma wakefield," Phys. Rev. Lett. **99**, 135001 (2007).
11. V. Malka, J. Faure, S. Hüller, V. T. Tikhonchuk, S. Weber, and F. Amiranoff, "Enhanced spatiotemporal laser-beam smoothing in gas-jet plasmas," Phys. Rev. Lett. **90**, 75002 (2003).
12. V. Malka, "Laser plasma accelerators," Phys. Plasmas **19**, 055501 (2012).
13. E. Esarey, C. Schroeder, and W. Leemans, "Physics of laser-driven plasma-based electron accelerators," Rev. Mod. Phys. **81**, 1229–1285 (2009).
14. A. J. Gonsalves, K. Nakamura, C. Lin, D. Panasenko, S. Shiraishi, T. Sokollik, C. Benedetti, C. B. Schroeder, C. G. R. Geddes, J. van Tilborg, J. Osterhoff, E. Esarey, C. Toth, and W. P. Leemans, "Tunable laser plasma accelerator based on longitudinal density tailoring," Nat. Phys. **7**, 862–866 (2011).
15. H. T. Kim, K. H. Pae, H. J. Cha, I. J. Kim, T. J. Yu, J. H. Sung, S. K. Lee, T. M. Jeong, and J. Lee, "Enhancement of electron energy to the multi-GeV regime by a dual-stage laser-wakefield accelerator pumped by petawatt laser pulses," Phys. Rev. Lett. **111**, 165002 (2013).
16. S. Chen, N. D. Powers, I. Ghebregziabher, C. M. Maharjan, C. Liu, G. Golovin, S. Banerjee, J. Zhang, N. Cunningham, A. Moorti, S. Clarke, S. Pozzi, and D. P. Umstadter, "MeV-energy x rays from inverse compton scattering with laser-wakefield accelerated electrons," Phys. Rev. Lett. **110**, 155003 (2013).
17. N. D. Powers, I. Ghebregziabher, G. Golovin, C. Liu, S. Chen, S. Banerjee, J. Zhang, and D. P. Umstadter, "Quasi-monoenergetic and tunable x-rays from a laser-driven Compton light source," Nat. Photonics **8**, 28–31 (2013).
18. K. Ta Phuoc, S. Corde, C. Thaury, V. Malka, A. Tafzi, J. P. Goddet, R. C. Shah, S. Sebban, and A. Rousse, "All-optical Compton gamma-ray source," Nat. Photonics **6**, 308–311 (2012).
19. C. Liu, G. Golovin, S. Chen, J. Zhang, B. Zhao, D. Haden, S. Banerjee, J. Silano, H. Karwowski, and D. Umstadter, "Generation of 9 MeV γ-rays by all-laser-driven Compton scattering with second-harmonic laser light," Opt. Lett. **39**, 4132–4135 (2014).
20. H. Kleine, H. Grönig, and K. Takayama, "Simultaneous shadow, Schlieren and interferometric visualization of compressible flows," Opt. Lasers Eng. **44**, 170–189 (2006).
21. N. Lemos, N. Lopes, J. M. Dias, and F. Viola, "Design and characterization of supersonic nozzles for wide focus laser-plasma interactions," Rev. Sci. Instrum. **80**, 103301 (2009).
22. K. Schmid and L. Veisz, "Supersonic gas jets for laser-plasma experiments," Rev. Sci. Instrum. **83**, 053304 2012.
23. S. Semushin and V. Malka, "High density gas jet nozzle design for laser target production," Rev. Sci. Instrum. **72**, 2961–2965 (2001).
24. F. Sylla, M. Veltcheva, S. Kahaly, A. Flacco, and V. Malka, "Development and characterization of very dense submillimetric gas jets for laser-plasma interaction," Rev. Sci. Instrum. **83**, 033507 (2012).
25. T. Auguste, M. Bougeard, E. Caprin, P. D'Oliveira, and P. Monot, "Characterization of a high-density large scale pulsed gas jet for laser–gas interaction experiments," Rev. Sci. Instrum. **70**, 2349–2354 (1999).
26. V. Malka, C. Coulaud, J. P. Geindre, V. Lopez, Z. Najmudin, D. Neely, and F. Amiranoff, "Characterization of neutral density profile in a wide range of pressure of cylindrical pulsed gas jets," Rev. Sci. Instrum. **71**, 2329–2333 (2000).
27. B. Landgraf, M. Schnell, A. Sävert, M. C. Kaluza, and C. Spielmann, "High resolution 3D gas-jet characterization," Rev. Sci. Instrum. **82**, 083106 (2011).
28. R. Gordon, R. Bender, and G. T. Herman, "Algebraic Reconstruction Techniques (ART) for three-dimensional electron microscopy and X-ray photography," J. Theoret. Biol. **29**, 471–481 (1970).
29. C. Söller, R. Wenskus, P. Middendorf, G. E. A. Meier, and F. Obermeier, "Interferometric tomography for flow visualization of density fields in supersonic jets and convective flow," Appl. Opt. **33**, 2921 (1994).
30. P. Gilbert, "Iterative methods for the three-dimensional reconstruction of an object from projections," J. Theoret. Biol. **36**, 105–117 (1972).

31. R. Azambuja, M. Eloy, G. Figueira, and D. Neely, "Three-dimensional characterization of high-density non-cylindrical pulsed gas jets," J. Phys. D **32**, L35–L43 (1999).
32. M. Burza, A. Gonoskov, K. Svensson, F. Wojda, A. Persson, M. Hansson, G. Genoud, M. Marklund, C.-G. Wahlström, and O. Lundh, "Laser wakefield acceleration using wire produced double density ramps," Phys. Rev. ST Accel. Beams **16**, 011301 (2013).
33. K. Schmid, A. Buck, C. Sears, J. Mikhailova, R. Tautz, D. Herrmann, M. Geissler, F. Krausz, and L. Veisz, "Density-transition based electron injector for laser driven wakefield accelerators," Phys. Rev. ST Accel. Beams **13**, 1–5 (2010).
34. Y.-C. Ho, T.-S. Hung, J.-G. Jhou, H. Qayyum, W.-H. Chen, H.-H. Chu, J.-Y. Lin, J. Wang, and S.-Y. Chen, "Induction of electron injection and betatron oscillation in a plasma-waveguide-based laser wakefield accelerator by modification of waveguide structure," Phys. Plasmas **20**, 083104 (2013).
35. S. Fourmaux, K. Ta Phuoc, P. Lassonde, S. Corde, G. Lebrun, V. Malka, A. Rousse, and J. C. Kieffer, "Quasi-monoenergetic electron beams production in a sharp density transition," Appl. Phys. Lett. **101**, 111106 (2012).
36. T.-Y. Chien, C.-L. Chang, C.-H. Lee, J.-Y. Lin, J. Wang, and S.-Y. Chen, "Spatially localized self-injection of electrons in a self-modulated laser-wakefield accelerator by using a laser-induced transient density ramp," Phys. Rev. Lett. **94**, 115003 (2005).
37. A. Buck, J. Wenz, J. Xu, K. Khrennikov, K. Schmid, M. Heigoldt, J. M. Mikhailova, M. Geissler, B. Shen, F. Krausz, S. Karsch, and L. Veisz, "Shock-front injector for high-quality laser-plasma acceleration," Phys. Rev. Lett. **110**, 185006 (2013).
38. S. Y. Kalmykov, X. Davoine, and B. A. Shadwick, "All-optical control of electron self-injection in millimeter-scale, tapered dense plasmas," Nucl. Instrum. Methods Phys. Res. Sect. A **740**, 266–272 (2013).
39. A. Pukhov, "Control of laser-wakefield acceleration by the plasma-density profile," Phys. Rev. E **77**, 025401 (2008).
40. P. Sprangle, B. Hafizi, J. Peñano, R. Hubbard, A. Ting, C. Moore, D. Gordon, A. Zigler, D. Kaganovich, and T. Antonsen, "Wakefield generation and GeV acceleration in tapered plasma channels," Phys. Rev. E **63**, 1–11 (2001).
41. G. Golovin, S. Chen, N. Powers, C. Liu, S. Banerjee, J. Zhang, M. Zeng, Z. Sheng, and D. Umstadter, "Tunable monoenergetic electron beams from independently controllable laser-wakefield acceleration and injection," Phys. Rev. ST Accel. Beams **18**, 011301 (2015).
42. D. C. Ghiglia and M. D. Pritt, *Two-Dimensional Phase Unwrapping: Theory, Algorithms, and Software* (Wiley, 1998).
43. M. Born and E. Wolf, *Principles of Optics*, 7th ed. (Cambridge University, 1999), pp. 92–95.
44. R. M. G. M. Trines, R. Bingham, Z. Najmudin, S. Mangles, L. O. Silva, R. Fonseca, and P. A. Norreys, "Electron trapping and acceleration on a downward density ramp: a two-stage approach," New J. Phys. **12**, 045027 (2010).
45. S. Bulanov, N. Naumova, F. Pegoraro, and J. Sakai, "Particle injection into the wave acceleration phase due to nonlinear wake wave breaking," Phys. Rev. E **58**, R5257–R5260 (1998).